

Bose-Einstein condensate in Bloch bands with an off-diagonal periodic potentialYue-Xin Huang,¹ Wei Feng Zhuang,¹ Xiang-Fa Zhou,^{1,2,3} Han Pu,⁴ Guang-Can Guo,^{1,2,3} and Ming Gong^{1,2,3,*}¹CAS Key Laboratory of Quantum Information, University of Science and Technology of China, Hefei, 230026, China²Synergetic Innovation Center of Quantum Information and Quantum Physics, University of Science and Technology of China, Hefei, Anhui 230026, China³CAS Center For Excellence in Quantum Information and Quantum Physics, University of Science and Technology of China, Hefei, 230026, China⁴Department of Physics and Astronomy, Rice University, Houston, Texas 77005, USA

(Received 22 March 2019; revised manuscript received 23 September 2019; published 8 November 2019)

We report on the Bose-Einstein condensate in the Bloch bands with off-diagonal periodic potential (ODPP), which simultaneously plays the role of spin-orbit coupling and Zeeman field. This model can be realized using two independent Raman couplings in the same three-level system, in which the time-reversal symmetry ensures the energy degeneracy between the two states with opposite momenta. We find that these two Raman couplings can be used to tune the spin polarization in momentum space, thus greatly modifying the effective scatterings over the Bloch bands. We observe a transition from the Bloch plane wave phase with condensate at one wave vector to the Bloch stripe phase with condensate at the two Bloch states with opposite wave vectors. These two phases will exhibit different spin textures and density modulations in real space, which are totally different from that in free space. In momentum space, multiple peaks differing by some reciprocal lattice vectors can be observed in both phases, reflecting the periodic structure of the ODPP. A three-band effective model is proposed to understand these observations. This ODPP will never approach the tight-binding limit, thus can provide an alternative platform in the investigations of various physics, such as collective excitations, polaron, and topological superfluids, over the Bloch bands.

DOI: [10.1103/PhysRevA.100.053606](https://doi.org/10.1103/PhysRevA.100.053606)**I. INTRODUCTION**

Spin-orbit coupling (SOC) plays an important role in many important concepts in condensed matter physics [1–4]. This interaction has been widely explored in ultracold atoms [5–10]. In Bose gases, it could be used to realize the Bose-Einstein condensate (BEC) [11,12] with finite momentum, which belongs to either the plane wave phase or the stripe phase [13–15], depending strongly on the interparticle and intraparticle interaction strengths. The spin dipole in this system will also exhibit some exotic behaviors in quench dynamics [16]. In Fermi gases, it can be used for the realization of topological superfluids [2,17–22] and the associated Majorana zero modes [23–25], due to the effective p -wave pairing at the Fermi surface. By carefully engineering the interaction, this system may also be used to create different types of gapless superfluids [26–29]. To date, both the one- [30] and two-dimensional SOC have been realized with Bosons [31] and Fermions [32]. In these experiments, the SOC is realized by the Raman coupling [7,33–36], which can be brought into Rashba or Dresselhaus SOC by a unitary transformation. These progresses open an avenue for searching of exotic phases in degenerate gases [30,37–42].

In this work, we consider the fate of a BEC in the Bloch bands with off-diagonal periodic potential (ODPP), which plays the role of SOC and Zeeman field simultaneously. This

potential can be realized using three laser beams coupled to the same three-level system (in Λ configuration), which forms two independent Raman couplings. In this model the position of the local energy minima and their corresponding spin textures can be tuned by the two Raman couplings, which in turn greatly influence the scatterings of the Bloch states. This model exhibits rich phase structures in both the single-particle band structure and the interacting condensates. Especially, we find a transition from the spin-imbalanced Bloch plane wave (BPW) phase condensed at one Bloch wave vector \mathbf{k}_0 to the spin-balanced Bloch stripe (BST) phase condensed at two vectors $\pm\mathbf{k}_0$ in the case with time-reversal (TR) symmetry. These two phases exhibit multiple peaks differ by several reciprocal lattice vectors in momentum space. The phase transition between these two phases can be controlled by the relative intensity of these two Raman coupling strengths but not their relative phase. Meanwhile, both phases will exhibit some intriguing spin textures and density modulations in real space. Thus, these two phases will have features that are totally different from the case with Rashba SOC in free space [5–10]. This platform also serves as an interesting model for exploring of various physics in the Bloch bands.

II. MODEL AND HAMILTONIAN

We consider a ^{87}Rb BEC in a weak trap [see Fig. 1(a)]. Three laser beams are used to couple the ground-state manifold $|F = 1, m_F\rangle$ to the excited-state manifold to construct two independent Raman couplings. Here laser beam L_3 is

*gongm@ustc.edu.cn

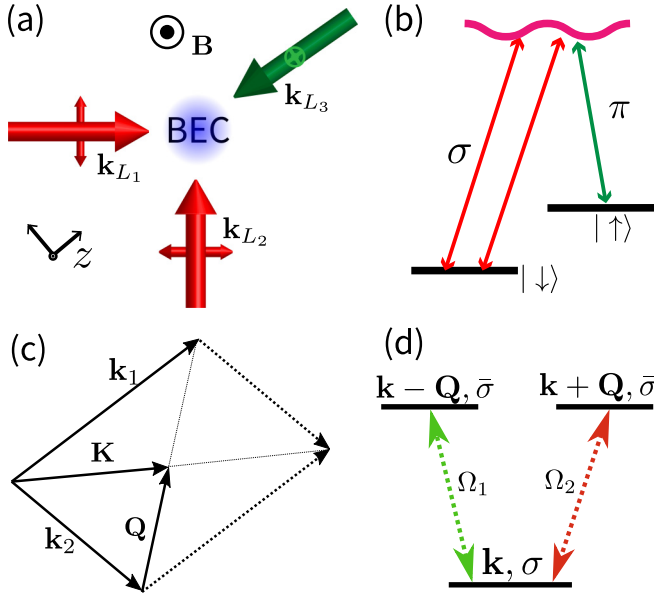


FIG. 1. (a) Setup for the ODPP. The laser L_1 with frequency ω_1 is linearly polarized along the z direction, and the two lasers $L_{2/3}$ with identical frequency ω_2 are orthogonally polarized in the x - y plane. (b) These three laser beams form two independent Raman couplings in the same three-level system. (c) Momentum transfer in these two Raman couplings with $\mathbf{k}_i \equiv \mathbf{k}_{L_i} - \mathbf{k}_{L_3}$ for $i = 1, 2$. (d) The plane wave \mathbf{k} with spin σ is coupled to the two other plane wave vectors $\mathbf{k} \pm \mathbf{Q}$ with opposite spin $\bar{\sigma}$ by Ω_1 and Ω_2 , respectively.

linearly polarized along the $\hat{\mathbf{z}}$ direction (π transition) and L_1 and L_2 from the same laser source with identical frequency are polarized in the x - y plane (σ transition). We assume that the polarization of the L_1 and L_2 beams are mutually orthogonal to avoid interference (see details in Appendix A). These two couplings are accompanied by a momentum transfer $\tilde{\mathbf{k}}_i \equiv \mathbf{k}_{L_i} - \mathbf{k}_{L_3}$ for $i = 1, 2$. By labeling $|\downarrow\rangle = |1, -1\rangle$ and $|\uparrow\rangle = |1, 0\rangle$, we have the following Hamiltonian:

$$H = \int d\mathbf{r} \Psi^\dagger(\mathbf{r}) [\mathcal{H}(\mathbf{r}) + \mathcal{V}_{\text{trap}}(\mathbf{r})] \Psi(\mathbf{r}). \quad (1)$$

By eliminating the excited bands in the large detuning limit (see details in Appendix A), we obtain the following single-particle Hamiltonian:

$$\mathcal{H}(\mathbf{r}) = \begin{pmatrix} \frac{\tilde{\mathbf{p}}^2}{2m} + \tilde{\delta} & \sum_{j=1,2} \tilde{\Omega}_j e^{i\tilde{\mathbf{k}}_j \cdot \tilde{\mathbf{r}}} \\ \sum_{j=1,2} \tilde{\Omega}_j^* e^{-i\tilde{\mathbf{k}}_j \cdot \tilde{\mathbf{r}}} & \frac{\tilde{\mathbf{p}}^2}{2m} - \tilde{\delta} \end{pmatrix}, \quad (2)$$

under basis $\Psi(\mathbf{r}) = [\psi_\uparrow(\mathbf{r}), \psi_\downarrow(\mathbf{r})]^T$. In this model, $\mathcal{V}_{\text{trap}}(\mathbf{r})$ is the harmonic trap potential, m is the mass, $\tilde{\mathbf{p}}$ is the momentum operator, $\tilde{\Omega}_j$ is the resonant Raman coupling strength, and $\tilde{\delta}$ is the detuning from Raman resonance. Note that the phases carried by $\tilde{\Omega}_{1,2}$ are always fixed as L_1 and L_2 originate from the same laser source, making our model immune to random phase fluctuation. When $\tilde{\Omega}_2$ (or $\tilde{\Omega}_1$) equals to zero, Eq. (2) is reduced to the model studied in the previous literature, which after a unitary transformation will yield an one-dimensional SOC [3,5,7]. In the presence of both Raman couplings, the phase carried by ODPP can no longer be gauged out.

In the following, we rescale the energy and momentum in units of recoil energy $E_r = \hbar^2 k_r^2 / 2m$ and recoil momentum

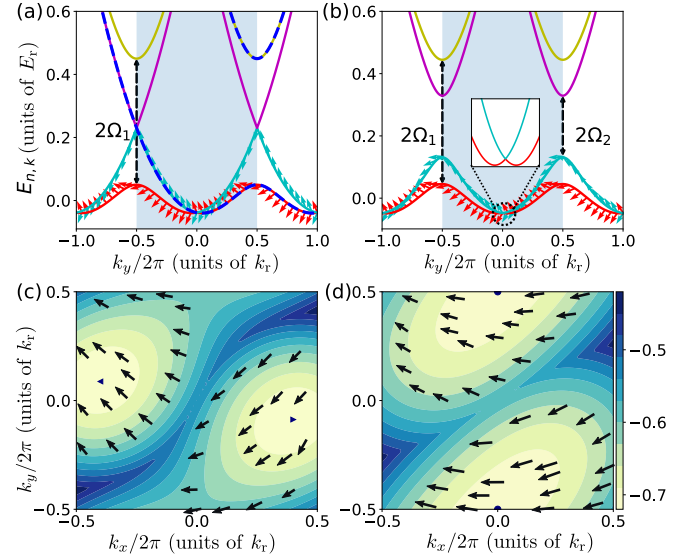


FIG. 2. (a) Energy spectrum with $\Omega_1 = 0.2$, $\Omega_2 = 0$ when $k_x = 0$, here the Ω_i have defined in unit of the recoil energy E_r . The blue dashed lines are obtained with $\tilde{\mathcal{H}}$, in which k_y has been shifted to match the bands obtained using Bloch theorem. (b) Spectrum with $\Omega_1 = 0.2$, $\Omega_2 = 0.1$ when $k_x = 0$. The inset shows the detail of the double minima. (c) Double minima spectrum in two dimension when $\Omega_1 = 0.6$ and $\Omega_2 = 0.2$. (d) Single minimum at $(0, \pi)$ with $\Omega_1 = 1.2$ and $\Omega_2 = 0.2$. The arrows in (c) and (d) represent the spin polarization in σ_x - σ_z space in momentum spacing, indicating of spin-momentum locking from two-dimensional SOC.

k_r [43], then we can define $\tilde{\delta} = \delta E_r$, $\tilde{\Omega}_j = \Omega_j E_r$, $\tilde{\mathbf{k}}_i = \mathbf{k}_i k_r$, $\tilde{\mathbf{K}} = \mathbf{K} k_r$, and $\tilde{\mathbf{Q}} = \mathbf{Q} k_r$, where $\mathbf{K} = \frac{\mathbf{k}_1 + \mathbf{k}_2}{2}$ and $\mathbf{Q} = \frac{\mathbf{k}_1 - \mathbf{k}_2}{2}$ [see Fig. 1(c)]. After a unitary transformation [5], we have

$$\mathcal{H}(\mathbf{r}) = \begin{pmatrix} (\mathbf{p} + \mathbf{K}/2)^2 + \delta & \Omega_1 e^{i\mathbf{Q} \cdot \mathbf{r}} + \Omega_2 e^{-i\mathbf{Q} \cdot \mathbf{r}} \\ \Omega_1^* e^{-i\mathbf{Q} \cdot \mathbf{r}} + \Omega_2^* e^{i\mathbf{Q} \cdot \mathbf{r}} & (\mathbf{p} - \mathbf{K}/2)^2 - \delta \end{pmatrix}. \quad (3)$$

The physical meaning now becomes clear. The global plane carried by the vector \mathbf{K} plays the role of one-dimensional SOC, and the ODPP, which represents a helical magnetic field with period determined by $2\pi/Q$ in real space, plays the role of spatially varying Zeeman field. However, it is more complicated because this helical magnetic field is coupled to the momentum, hence behaving as some kind of SOC. The two-dimensional nature of the SOC from the spin-momentum locking effect is shown in Figs. 2(c) and 2(d). The relative phase between the two Raman couplings can be gauged out by a position shift, thus it is unimportant. Hereafter we will focus on the case with $\delta = 0$, at which point the model is invariant under the anti-unitary transformation $\Theta = \sigma_x \mathcal{K}$, with \mathcal{K} being the complex conjugate operator. In the following, for simplicity, we only report the case of $|\mathbf{k}_1| = |\mathbf{k}_2|$, then \mathbf{K} is perpendicular to \mathbf{Q} . The case with two non-perpendicular vectors will be discussed elsewhere. In our simulation, we let $\mathbf{K} = K \hat{\mathbf{x}}$ and $\mathbf{Q} = Q \hat{\mathbf{y}}$, then the diagonal term represents the usual one-dimensional SOC as $k_x \sigma_z$ along the x direction.

The wave function can be written as [44]

$$\psi_{s,\mathbf{k}}(\mathbf{r}) = \sum_{\mathbf{G}} \phi_{s,\mathbf{k},\mathbf{G}} e^{i(\mathbf{k} + \mathbf{G}) \cdot \mathbf{r}}, \quad (4)$$

following the Bloch theorem, where $k_y \in [-Q/2, Q/2]$ and $\mathbf{G} = n\mathbf{Q}$ ($n \in \mathbb{Z}$) are the reciprocal lattice vectors. In this basis, the Hamiltonian can be written as $H_{\mathbf{k}} = \sum_{\mathbf{G}} \mathcal{H}_{\mathbf{k}}(\mathbf{G})$, where

$$\begin{aligned} \mathcal{H}_{\mathbf{k}}(\mathbf{G}) = & \sum_{s=\uparrow,\downarrow} \phi_{s,\mathbf{k},\mathbf{G}}^\dagger [(\mathbf{k} + \mathbf{G} + c_s \mathbf{K}/2)^2] \phi_{s,\mathbf{k},\mathbf{G}} \\ & + (\Omega_1 \phi_{\uparrow,\mathbf{k},\mathbf{G}}^\dagger \phi_{\downarrow,\mathbf{k},\mathbf{G}-\mathbf{Q}} + \Omega_2 \phi_{\uparrow,\mathbf{k},\mathbf{G}}^\dagger \phi_{\downarrow,\mathbf{k},\mathbf{G}+\mathbf{Q}} + \text{H.c.}), \end{aligned} \quad (5)$$

with $c_\uparrow = 1$ and $c_\downarrow = -1$. We see that the Ω_1 field couples $\phi_{\uparrow,\mathbf{k},\mathbf{G}}$ to $\phi_{\downarrow,\mathbf{k},\mathbf{G}-\mathbf{Q}}$, while the Ω_2 field couples $\phi_{\uparrow,\mathbf{k},\mathbf{G}}$ to $\phi_{\downarrow,\mathbf{k},\mathbf{G}+\mathbf{Q}}$ [see illustration in Fig. 1(d)]. In momentum space, one can define a TR operator $\Theta_{\text{tr}} = \mathbb{I}_{2n_c+1} \otimes \Theta$, with $\Theta_{\text{tr}} H_{\mathbf{k}} \Theta_{\text{tr}}^{-1} = H_{-\mathbf{k}}$ [45]. Moreover, the Hamiltonian can be made real if all $\Omega_i \in \mathbb{R}$ using the symmetry \mathcal{K} .

III. SINGLE-PARTICLE PHASE DIAGRAM

We first consider the single-particle spectra, as shown in Fig. 2. The case with $\Omega_2 = 0$ can be obtained exactly via an unitary transformation, which yields $\tilde{\mathcal{H}} = \mathbf{k}^2 + \sigma_z \mathbf{k} \cdot \mathbf{k}_1 + \Omega_1 \sigma_x$ and spectra $\epsilon_{\mathbf{k}\pm} = \mathbf{k}^2 \pm \sqrt{(\mathbf{k} \cdot \mathbf{k}_1)^2 + \Omega_1^2}$ [see the blue dashed lines in Fig. 2(a)]. However, by Bloch theorem, the dispersion in free space should be folded into the first BZ, in which the Raman coupling Ω_1 will open an energy gap between the ground state and the third excited band [see Fig. 2(a)]. The folded spectra form the first and second excited bands.

Next we switch on the second Raman coupling $\Omega_2 \neq 0$, and the corresponding Bloch bands are shown in Fig. 2(b). We see that this additional coupling can open an energy gap between the folded spectra at $k_y = \pm \frac{1}{2}$. The interplay between these two Raman couplings can greatly influence the spin texture in momentum space [46,47]. Two typical examples for the lowest band $E_{1,\mathbf{k}}$ from the Bloch wave functions are presented in Figs. 2(c) and 2(d), from which one can see that the position of the ground-state minima can be controlled in the whole BZ by tuning the two Raman coupling strengths. Moreover, the TR symmetry Θ_{tr} ensures $E_{n,\mathbf{k}} = E_{n,-\mathbf{k}}$.

The single-particle phase diagram is characterized by the position of the energy minima [see Fig. 3(a)], which exhibits a star structure. To understand this diagram, let us consider the limit that $|\Omega_1| \gg |\Omega_2|$, then by ignoring Ω_2 , the Hamiltonian can be written as $k^2 + (Qk_y + Kk_x)\sigma_z + \Omega_1 \sigma_x$, which exhibits two local minima when Ω_1 is small, and one minimum at $\mathbf{k} = 0$ when $|\Omega_1| \gg |Q\hat{y} + K\hat{x}|$. Noticed that the unitary transformation has introduced a momentum shift, thus the single minimum is shifted to $\mathbf{k} = (0, \pi)$. When $\Omega_1 = \pm\Omega_2$, which corresponds to the diagonal ($\Omega_1 = \Omega_2$) and off-diagonal ($\Omega_1 = -\Omega_2$) axes in Fig. 3(a) denoted by dashed lines, it will always exhibit two local minima even when Ω_1 becomes large. In this case, these two minima will never merge to a single minimum. Thus, by tuning these two Raman couplings, one can not only engineer the spin polarization, but also the position of the ground-state minima, which can influence the fate of the BEC over the Bloch bands.

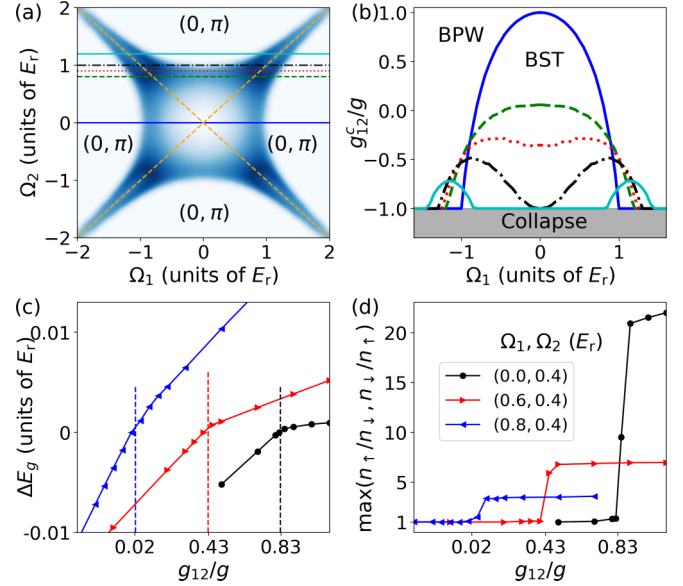


FIG. 3. (a) Single-particle phase diagram in the parameter space Ω_1 and Ω_2 . The color represents the distance between the two minima, thus the white color represents one local minimum. (b) The phase boundary between BPW ($g_1 > g_{12}^c$) and BST ($g_{12} < g_{12}^c$) influenced by the two Raman couplings for the three horizon lines in (a), with $\Omega_2 = (0, 0.8, 0.9, 1.0, 1.2)$. The system collapses when $g_{12}/g < -1$. (c, d) Ground-state energy $\Delta E_g = E_g(g_{12}) - E_g(g_{12}^c)$ and spin polarization across the phase boundaries for three typical parameters.

IV. BEC OVER THE BLOCH BANDS AND PHASE DIAGRAM

With these features, we naturally ask the question that what will happen to the condensate in these Bloch bands? From the viewpoint of plane wave basis, this condensate occupies multiple momenta simultaneously. In the weak interacting limit, one expects the atoms to be condensed at the ground state(s) of the Bloch bands. We consider the following interaction [48],

$$\mathcal{V}_1 = \int d\mathbf{r} \{g[n_\uparrow^2(\mathbf{r}) + n_\downarrow^2(\mathbf{r})] + 2g_{12}n_\uparrow(\mathbf{r})n_\downarrow(\mathbf{r})\}. \quad (6)$$

Then we expand the wave function in terms of the Bloch basis $\phi_{n,\mathbf{k}}$. The condensate should occur at one momentum with $\mathbf{k} = -\mathbf{k}_0$ or \mathbf{k}_0 , or both of them. By only considering the scattering at these two points, we obtain an effective interaction over the Bloch bands,

$$\mathcal{V}_1 = U_{\mathbf{k}_0}(n_{\mathbf{k}_0} + n_{-\mathbf{k}_0})^2 + (V_{\mathbf{k}_0} - 2U_{\mathbf{k}_0})n_{\mathbf{k}_0}n_{-\mathbf{k}_0}. \quad (7)$$

Here the two coefficients g and g_{12} will contribute to both $U_{\mathbf{k}_0}$ and $V_{\mathbf{k}_0}$ in a linear but complicated way. In general, $U_{\mathbf{k}_0} > 0$, thus the sign of the second term determines the fate of condensate [14,40,49,50]. It occupies a single Bloch vector (for the BPW phase) when $V_{\mathbf{k}_0} - 2U_{\mathbf{k}_0} > 0$ and two Bloch vectors (for the BST phase) with equal population of $\pm\mathbf{k}_0$ when $V_{\mathbf{k}_0} - 2U_{\mathbf{k}_0} < 0$. With this criterion, we determine the phase boundary between these two phases in Fig. 3(b). Strikingly, we find that the spin polarizations can fundamentally influence the scatterings in the condensate, thus dramatically influence the phase boundaries between these phases. The change of this

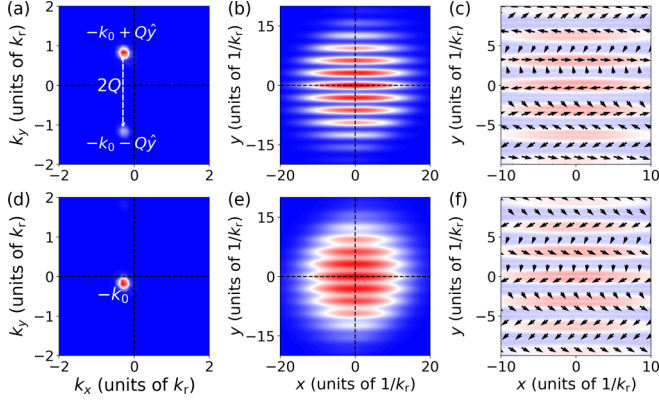


FIG. 4. Properties of the BPW phase. (a) and (d) Wave function in momentum space for spin up and spin down components, respectively. (b) and (e) The corresponding wave functions for these two components in real space. Spin polarization in $\sigma_x - \sigma_y$ space and $\sigma_x - \sigma_z$ space are shown in (c) and (f). These results are obtained from GPE simulation with parameters: $\Omega_1 = 0.4$, $\Omega_2 = 0.8$, $g_{12}/g = 0.1$, and $\mathbf{k}_0 \approx (0.30, 0.15)$.

boundary is further confirmed by numerical simulation using Gross-Pitaevskii equation (GPE); see Figs. 3(c) and 3(d), in which during the transition from the BPW phase to the BST phase, dramatic changes in ground-state energy $E_g - E_g(g_{12}^c)$ and total spin polarization can be observed.

In the special condition with only one Raman coupling, say $\Omega_2 = 0$. We find $U_{\mathbf{k}_0} = g - \eta g + \eta g_{12}$ and $V_{\mathbf{k}_0} - 2U_{\mathbf{k}_0} = (6\eta - 2)g + (2 - 2\eta)g_{12}$, where $\eta = 2\Omega_1^2/k_1^4$. The phase boundary is given by [14,51]

$$\frac{g_{12}^c}{g} = \frac{2 - 6\eta}{2 - 2\eta} = \frac{k_1^4 - 6\Omega_1^2}{k_1^4 - 2\Omega_1^2}, \quad \text{for } |\Omega_1| < k_1^2/2, \quad (8)$$

which corresponds to the blue solid line in Fig. 3(b). This boundary can be used to explain the four limits that when $\Omega_1 = 0$, $\Omega_2^c = \pm 1$, and when $\Omega_2 = 0$, $\Omega_1^c = \pm 1$.

V. SPIN TEXTURES, DENSITY MODULATIONS, AND EFFECTIVE HAMILTONIAN

In the BPW phase, only one Bloch wave vector \mathbf{k}_0 is occupied. We find that one of the spin components will occupy one momentum \mathbf{k}_0 , and the other component occupies two momenta $\mathbf{k}_0 \pm \mathbf{Q}$. The other momenta such as $\mathbf{k}_0 + n\mathbf{Q}$ for $n \neq \pm 1$ are presented but not discernible in the present plot. By keeping only these three components as $(\phi_{\downarrow, \mathbf{k}_0, -\mathbf{Q}}, \phi_{\uparrow, \mathbf{k}_0, 0}, \phi_{\downarrow, \mathbf{k}_0, \mathbf{Q}})^T$, we obtain an effective Hamiltonian as

$$\mathcal{H}_{\text{eff}}(\mathbf{k}_0) = \begin{pmatrix} \epsilon_{\mathbf{k}_0 - \mathbf{Q}}^{-1} & \Omega_1 & 0 \\ \Omega_1^* & \epsilon_{\mathbf{k}_0}^0 & \Omega_2 \\ 0 & \Omega_2^* & \epsilon_{\mathbf{k}_0 + \mathbf{Q}}^+ \end{pmatrix}, \quad (9)$$

where $\epsilon_{\mathbf{k}}^0 = (\mathbf{k}_x + K/2)^2 + \mathbf{k}_y^2$ and $\epsilon_{\mathbf{k}}^{\pm 1} = (\mathbf{k}_x - K/2)^2 + \mathbf{k}_y^2$. We can use this effective Hamiltonian to understand our numerical results from GPE simulation. In Fig. 4, the two Raman couplings have different strengths, thus the two peaks in Fig. 4(a) have different intensities. We find the ground state is $(-0.154, 0.897, -0.413)^T$, thus the intensity ratio between

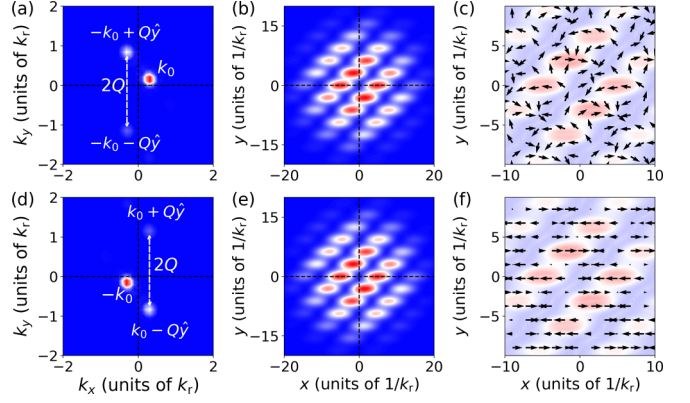


FIG. 5. Properties of the BST phase with parameters $\Omega_1 = 0.4$, $\Omega_2 = 0.8$, $g_{12}/g = -0.1$, $\mathbf{k}_0 \approx (0.30, 0.15)$. The other parameters are the same as that in Fig. 4.

these two peaks $\mathbf{k}_0 \pm \mathbf{Q}$ is $0.413/0.154 = 2.69$, while the GPE gives 2.58. The intensity ratio between \mathbf{k}_0 and $\mathbf{k}_0 + \mathbf{Q}$ is $0.897/0.413 \approx 2.17$, while the GPE gives 2.24. The interference between different momenta can give rise to density modulation in real space [see Figs. 4(b) and 4(e), and more numerical data can be found in Appendix B], while in free space, this kind of modulation is absent. Furthermore, this phase will also exhibit some interesting spin textures in real space as shown in Figs. 4(c) and 4(f). We then compare these features to that in BST phase in Fig. 5, in which each component will exhibit three peaks in momentum space due to occupation of both wave vectors $\pm \mathbf{k}_0$. As a result, the density modulations and spin textures in real space are also totally different. Note that in the BST phase, the total spin is balanced, thus $\langle \psi_{\mathbf{k}_0} | \sigma_z | \psi_{\mathbf{k}_0} \rangle = 0$ [see Fig. 5(f)]. These features can be understood from two copies of model Eq. (9), i.e.,

$$\mathcal{H} = \text{diag}[\mathcal{H}_{\text{eff}}(\mathbf{k}_0), \mathcal{H}_{\text{eff}}(-\mathbf{k}_0)]. \quad (10)$$

Due to the same parameters Ω_1 and Ω_2 used in both figures, they should have the same intensities. The case with $\Omega_1 = \Omega_2 = 1.0$ for different g , which exhibit the similar interference features, are presented in Appendix B. These features provide smoking gun evidences in experiments to identify these two phases.

VI. CONCLUSION AND DISCUSSION

Our model possesses some features similar to that of two-dimensional SOC. The real representation of $\mathcal{H}_{\mathbf{k}}$ ensure that the geometry phase around any closed loop exactly vanish. However, by applying an in-plane Zeeman field $h_x \sigma_x$, which still respects Θ_{tr} symmetry but breaks the \mathcal{K} symmetry, we can awake the two-dimensional nature of SOC with a finite geometry phase. While this feature is not essential for BEC in Bloch bands, it may be important for the realization of topological superfluids in Fermi gases, in which the BCS pairing [52–55] is ensured by Θ_{tr} symmetry.

To conclude, we demonstrate some exotic condensates in the Bloch bands with ODPP realized using three laser beams coupled to the same three-level system. With this potential, the single-particle spectrum exhibit different and more complicated structure with the one-dimension SOC, resulting in

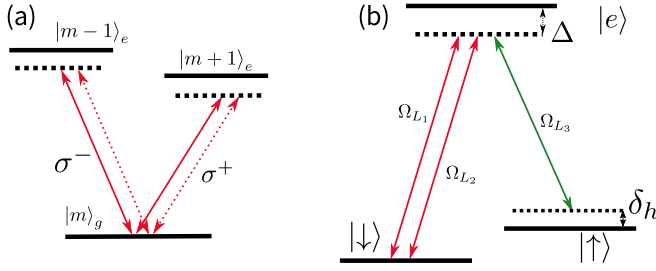


FIG. 6. (a) Two lasers, polarize along the \hat{x} and \hat{y} directions, couple the ground state $|m\rangle_g$ to the excited states $|m-1\rangle_e$ and $|m+1\rangle_e$. Here the ground state $|m\rangle_g$ denotes hyperfine state $5^2S_{1/2}$ with $F=1$, $m_F=m$, and the excited state $|m\rangle_e$ denotes $5^2P_{1/2}$ with $F=1$, $m_F=m$ [62]. The solid and dashed lines denote the two lasers, respectively. (b) Two independent Raman couplings in the same three-level system. Lasers L_1 and L_2 , which polarize in the \hat{x} - \hat{y} plane, couple $|\downarrow\rangle$ to $|e\rangle$, while Laser L_3 linearly polarizes along the \hat{z} direction, couples $|\uparrow\rangle$ to $|e\rangle$.

the modulation of the distribution of the condensate in the plane wave and stripe phases. By involving more lasers from the same source, different forms of ODPP can be realized. This kind of potential can never approach the tight-binding limit, thus it enables us to simulate some intriguing physics beyond the realm of condensed matter physics, which should be an important goal in AMO physics. This ODPP can change the interactions over the Bloch bands and thus may lead to alternative physics, such as collective oscillation and damping of condensate [56–58], polaron physics [59–61], topological superfluids [28,29], and their quench dynamics.

ACKNOWLEDGMENTS

This work is supported by the National Key Research and Development Program in China (Grants No. 2017YFA0304504 and No. 2017YFA0304103) and the National Natural Science Foundation of China (NSFC) (Grants No. 11774328 and No. 11774332). M.G. is also supported by the National Youth Thousand Talents Program and USTC startup funding. H.P. is supported from the U.S. NSF and the Welch Foundation (Grant No. C-1669).

APPENDIX A: DERIVATION OF THE EFFECTIVE HAMILTONIAN

1. Absence of interference between two orthogonal laser beams

First, we show that two orthogonal linear polarized laser beams do not have interference effect. Let us assume the two lasers are polarized along the \hat{x} and \hat{y} directions [see Fig. 6(a)], so their electric field components can be written as

$$\mathbf{E}_1 = \varepsilon_1 e^{i\mathbf{q}_1 \cdot \mathbf{r} - i\omega t} \hat{x} \quad \mathbf{E}_2 = \varepsilon_2 e^{i\mathbf{q}_2 \cdot \mathbf{r} - i\omega t} \hat{y}, \quad (\text{A1})$$

where \mathbf{q}_1 and \mathbf{q}_2 denote the momenta of the two lasers and ω is the frequency of the two lasers. The magnetic field along the \hat{z} direction sets the spin polarization axis, then we have

$$\hat{x} = \sigma^+ + \sigma^- \quad \hat{y} = -i\sigma^+ + i\sigma^-. \quad (\text{A2})$$

As a result, both lasers can induce σ^+ and σ^- transitions. We can define the dipole moment for σ^\pm transitions as $\mathbf{d}_\pm = d_0 \sigma^\pm$. In the large single photon detuning limit, the

excited states $|m \pm 1\rangle_e$ can be adiabatically eliminated, resulting in the AC Stark shift as

$$\begin{aligned} & \frac{1}{\Delta} [|\mathbf{d}_+ \cdot (\mathbf{E}_1 + \mathbf{E}_2)|^2 + |\mathbf{d}_- \cdot (\mathbf{E}_1 + \mathbf{E}_2)|^2] \\ &= \frac{d_0^2}{\Delta} (|\varepsilon_1 e^{i\mathbf{q}_1 \cdot \mathbf{r}} - i\varepsilon_2 e^{i\mathbf{q}_2 \cdot \mathbf{r}}|^2 + |\varepsilon_1 e^{i\mathbf{q}_1 \cdot \mathbf{r}} + i\varepsilon_2 e^{i\mathbf{q}_2 \cdot \mathbf{r}}|^2) \\ &= \frac{2d_0^2}{\Delta} (\varepsilon_1^2 + \varepsilon_2^2). \end{aligned} \quad (\text{A3})$$

In the above calculation we can safely assume that the σ^+ and σ^- transitions have the same detuning since the Zeeman splitting with the order of MHz, is much smaller than the detuning Δ with the order of GHz. Thus, we see that the interference between these two Raman couplings are exactly canceled and the lowest state $|m\rangle_g$ only feels a constant AC Stark shift. This picture is true even by considering all hyperfine levels.

2. The effective Hamiltonian

Next, we derive the effective Hamiltonian using the three-level system in Fig. 6(b). In this setup, the two lasers L_1 and L_2 come from the same source and polarize linearly in the \hat{x} - \hat{y} plane and the third laser L_3 polarizes along the \hat{z} direction. We only consider a three-level system, although in ultracold atoms, the excited manifolds contains a lot of energy levels [62]. However, only one of them is energetically allowed in the two-photon Raman coupling, and all the other couplings only contributes to an effective Zeeman field to the two ground-state energy levels. The original Hamiltonian can be written as

$$\begin{aligned} H_{\text{orig}} &= \omega_\uparrow |\uparrow\rangle\langle\uparrow| + \omega_\downarrow |\downarrow\rangle\langle\downarrow| + \omega_e |e\rangle\langle e| \\ &+ [e^{-i\omega_{L_1} t} (\Omega_{L_1} e^{i\mathbf{k}_{L_1} \cdot \mathbf{r}} + \Omega_{L_2} e^{i\mathbf{k}_{L_2} \cdot \mathbf{r}}) |e\rangle\langle\downarrow| \\ &+ \Omega_{L_3} e^{-i\omega_{L_3} t + i\mathbf{k}_{L_3} \cdot \mathbf{r}} |e\rangle\langle\uparrow| + \text{H.c.}]. \end{aligned} \quad (\text{A4})$$

Here ω_{L_i} , Ω_{L_i} and \mathbf{k}_{L_i} denote the frequency, the Rabi frequency and the wave vector of laser L_i , respectively. Noticed that we have assumed $\omega_{L_1} = \omega_{L_2}$. With an unitary transformation

$$\mathcal{U}_R = \exp[i\omega_\downarrow t |\downarrow\rangle\langle\downarrow| + i(\omega_\uparrow + \delta_h) t |\uparrow\rangle\langle\uparrow| + i(\omega_\downarrow + \omega_{L_1}) t |e\rangle\langle e|], \quad (\text{A5})$$

the Hamiltonian can be rotated to a time-independent model as

$$\begin{aligned} H_{\text{rotate}} &= \mathcal{U}_R H_{\text{orig}} \mathcal{U}_R^\dagger + i \left(\frac{\partial}{\partial t} \mathcal{U}_R \right) \mathcal{U}_R^\dagger \\ &= \Delta |e\rangle\langle e| - \delta_h |\uparrow\rangle\langle\uparrow| + [(\Omega_{L_1} e^{i\mathbf{k}_{L_1} \cdot \mathbf{r}} + \\ &\quad \times \Omega_{L_2} e^{i\mathbf{k}_{L_2} \cdot \mathbf{r}}) |e\rangle\langle\downarrow| + \Omega_{L_3} e^{i\mathbf{k}_{L_3} \cdot \mathbf{r}} |e\rangle\langle\uparrow| + \text{H.c.}] \\ &\equiv H_0 + H_R, \end{aligned} \quad (\text{A6})$$

where $\Delta = \omega_e - \omega_\downarrow - \omega_{L_1}$, $\omega_\uparrow + \delta_h + \omega_{L_3} = \omega_{L_1} + \omega_\downarrow$, and $H_0 = \Delta |e\rangle\langle e| - \delta_h |\uparrow\rangle\langle\uparrow|$. Usually, the detuning Δ is about tens or hundreds of GHz in experiments, which is much larger than the Rabi frequency $\Omega_{L_i} = 1 \sim 10$ MHz [30]. We can safely eliminate the contribution from the excited state via the second-order perturbation theory [63]. To obtain the effective

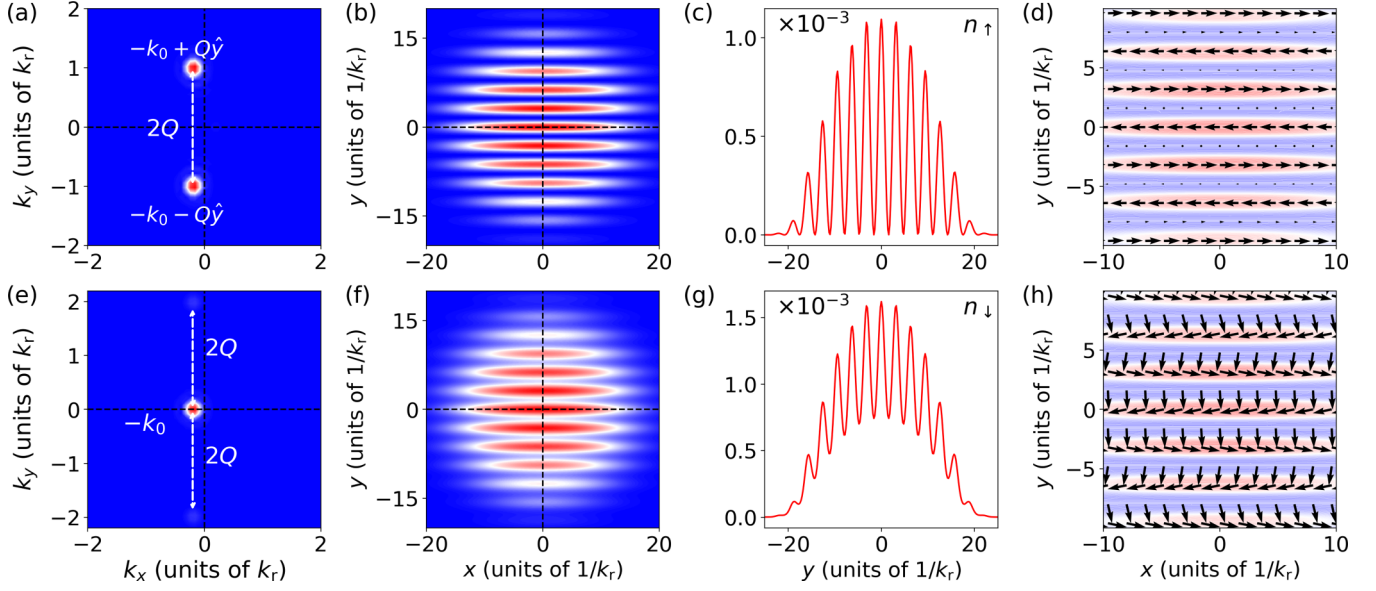


FIG. 7. Properties of the BPW when $\Omega_1 = \Omega_2 = 1.0$ and $g_{12}/g = -0.3$. (a) and (e) show the wave function in momentum space for spin up and spin down components, respectively. The corresponding wave functions in real space are given in (b) and (f). (c) and (g) show the densities of spin up and spin down components in the line of $x = 0$. (d) and (h) plot the spin polarization in $\sigma_x - \sigma_y$ and $\sigma_x - \sigma_z$ space. In (a), two major peaks are visible at $-\mathbf{k}_0 \pm Q\hat{y}$, while in (e), three peaks are visible at $-\mathbf{k}_0$ and $-\mathbf{k}_0 \pm 2Q\hat{y}$.

Hamiltonian, we define the projectors on the space of the lowest two states $\mathcal{P}_{\text{gs}} = |\downarrow\rangle\langle\downarrow| + |\uparrow\rangle\langle\uparrow|$ and the excited state $\mathcal{P}_{\text{ex}} = 1 - \mathcal{P}_{\text{gs}} = |e\rangle\langle e|$. Then, the effective Hamiltonian on the subspace $|\uparrow\rangle, |\downarrow\rangle$ can be written as [63]

$$\begin{aligned}
 H_{\text{pertur}} &= \mathcal{P}_{\text{gs}}(H_0 + H_{\text{R}})\mathcal{P}_{\text{gs}} + \mathcal{P}_{\text{gs}}H_{\text{R}}\mathcal{P}_{\text{ex}}\frac{1}{E_0 - \mathcal{P}_{\text{ex}}H_0\mathcal{P}_{\text{ex}}}\mathcal{P}_{\text{ex}}H_{\text{R}}\mathcal{P}_{\text{gs}} \\
 &= -\frac{1}{\Delta}\left[|\Omega_{L_1}|^2 + |\Omega_{L_2}|^2 + \Omega_{L_1}\Omega_{L_2}^*e^{i(\mathbf{k}_{L_1}-\mathbf{k}_{L_2})\cdot\mathbf{r}} + \Omega_{L_2}\Omega_{L_1}^*e^{i(\mathbf{k}_{L_2}-\mathbf{k}_{L_1})\cdot\mathbf{r}}\right]|\downarrow\rangle\langle\downarrow| - \left(\frac{1}{\Delta}|\Omega_{L_3}|^2 + \delta_h\right)|\uparrow\rangle\langle\uparrow| \\
 &\quad + \left[-\frac{\Omega_{L_1}^*\Omega_{L_3}}{\Delta}e^{-i(\mathbf{k}_{L_1}-\mathbf{k}_{L_3})\cdot\mathbf{r}}|\downarrow\rangle\langle\uparrow| - \frac{\Omega_{L_2}^*\Omega_{L_3}}{\Delta}e^{-i(\mathbf{k}_{L_2}-\mathbf{k}_{L_3})\cdot\mathbf{r}}|\downarrow\rangle\langle\uparrow| + \text{H.c.}\right]. \tag{A7}
 \end{aligned}$$

The amplitude of the effective Raman couplings, $\Omega_{L_i}^*\Omega_{L_3}/\Delta$ (for $i = 1, 2$) can range from 100 Hz to 10^4 Hz, or equivalently in the order from $0.1E_r$ to several E_r . In this effective model, the interference between the two lasers L_1 and L_2 can be exactly canceled, from our conclusion in Eq. (A3), thus it can be dropped out. Then we obtain an effective Hamiltonian as

$$\begin{aligned}
 H_{\text{eff}} &= \delta(|\uparrow\rangle\langle\uparrow| + |\downarrow\rangle\langle\downarrow|) + \delta(|\uparrow\rangle\langle\uparrow| - |\downarrow\rangle\langle\downarrow|) \\
 &\quad + (\Omega_1 e^{i\mathbf{k}_1\cdot\mathbf{r}} + \Omega_2 e^{i\mathbf{k}_2\cdot\mathbf{r}})|\uparrow\rangle\langle\downarrow| \\
 &\quad + (\Omega_1^* e^{-i\mathbf{k}_1\cdot\mathbf{r}} + \Omega_2^* e^{-i\mathbf{k}_2\cdot\mathbf{r}})|\downarrow\rangle\langle\uparrow|, \tag{A8}
 \end{aligned}$$

where we have defined

$$\delta = -(|\Omega_{L_3}|^2/\Delta + \delta_h)/2, \tag{A9}$$

$$\Omega_i = -\Omega_{L_i}\Omega_{L_3}^*/\Delta, \tag{A10}$$

and $\mathbf{k}_i = \mathbf{k}_{L_i} - \mathbf{k}_{L_3}$, with $i = 1, 2$. This is the expression used in the main text. Throughout this work, we let $\delta = 0$; while the result with $\delta \neq 0$ will be published elsewhere.

APPENDIX B: PHASES WITH $\Omega_1 = \Omega_2 = 1.0$ AND ANALYSIS USING A FIVE-BAND MODEL

We aim to provide some more numerical results from GPE simulation for the properties of BPW and BST phases discussed in the main text. When $\Omega_1 = \Omega_2 = 1.0$, the condensates happen at $\mathbf{k}_0 = (0.2, 0)$ and $-\mathbf{k}_0 = (-0.2, 0)$. The critical boundary is determined to be $g_{12}^2/g = -0.529$ from the simulation of $U_{\mathbf{k}_0}$ and $V_{\mathbf{k}_0}$ [see Eq. (7) in the main text]. Our numerical results for the BPW phase and BST phase are presented in Fig. 7) and Fig. 8, respectively. In this regime, we find that the $\pm\mathbf{k}_0 \pm 2\mathbf{Q}$ is visible, thus one need a 5×5 model, under the basis of $(\phi_{\uparrow, \mathbf{k}_0, -2\mathbf{Q}}, \phi_{\downarrow, \mathbf{k}_0, -\mathbf{Q}}, \phi_{\uparrow, \mathbf{k}_0, 0}, \phi_{\downarrow, \mathbf{k}_0, \mathbf{Q}}, \phi_{\uparrow, \mathbf{k}_0, 2\mathbf{Q}})^T$, to more accurately characterize the properties of these two phases, which can be written as follows:

$$H_{\mathbf{k}_0} = \begin{pmatrix} \epsilon_{\mathbf{k}_0, -2\mathbf{Q}}^{\uparrow} & \Omega_2 & 0 & 0 & 0 \\ \Omega_2 & \epsilon_{\mathbf{k}_0, -\mathbf{Q}}^{\downarrow} & \Omega_1 & 0 & 0 \\ 0 & \Omega_1 & \epsilon_{\mathbf{k}_0}^{\uparrow} & \Omega_2 & 0 \\ 0 & 0 & \Omega_2 & \epsilon_{\mathbf{k}_0, \mathbf{Q}}^{\downarrow} & \Omega_1 \\ 0 & 0 & 0 & \Omega_1 & \epsilon_{\mathbf{k}_0, 2\mathbf{Q}}^{\uparrow} \end{pmatrix}, \tag{B1}$$

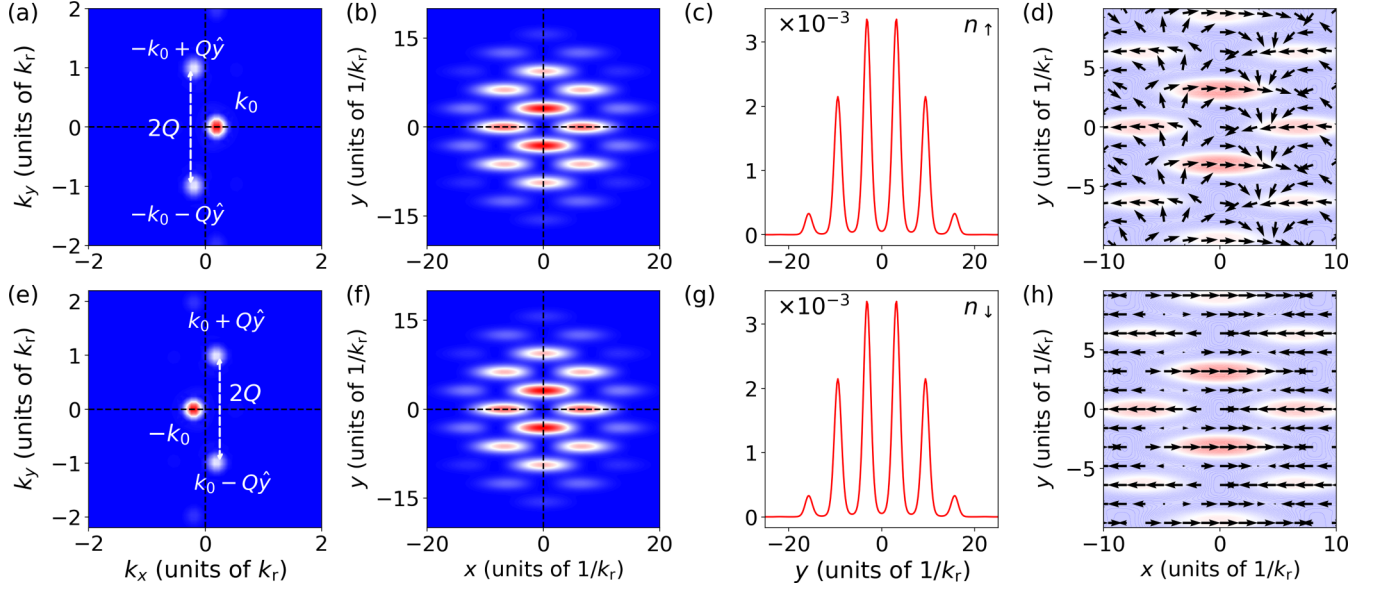


FIG. 8. Properties of the BST phase when $\Omega_1 = \Omega_2 = 1.0$ and $g_{12}/g = -0.7$. (a) and (e) show the wave function in momentum space for spin up and spin down components, respectively. The corresponding wave function in real space are presented in (b) and (f). (c) and (g) show the densities of spin up and spin down components in the line of $x = 0$. (d) and (h) plot the spin polarization in $\sigma_x - \sigma_y$ and $\sigma_x - \sigma_z$ space. In (a), five peaks can be found at \mathbf{k}_0 , $-\mathbf{k}_0 \pm Q\hat{y}$, $\mathbf{k}_0 \pm 2Q\hat{y}$. The peaks at $\mathbf{k} = \mathbf{k}_0 \pm 2Q\hat{y}$ is about one tenth in amplitude of the peaks at \mathbf{k}_0 . In (e), there are also five peaks at $-\mathbf{k}_0$, $\mathbf{k}_0 \pm Q\hat{y}$, $-\mathbf{k}_0 \pm 2Q\hat{y}$, just in the opposite position of the peaks in (a).

where

$$\epsilon_{\mathbf{k}}^{\uparrow} = (k_x + K/2)^2 + k_y^2, \quad (\text{B2})$$

$$\epsilon_{\mathbf{k}}^{\downarrow} = (k_x - K/2)^2 + k_y^2. \quad (\text{B3})$$

For the parameters $\Omega_1 = \Omega_2 = 1.0$, $K = 1$, $Q = 1$ and $-\mathbf{k}_0 = (-0.2, 0)$, we can get the eigenvector of the lowest state as $(0.0786, -0.388, 0.828, -0.388, 0.0786)$. So the ratio between the peaks at $-\mathbf{k}_0$ and $-\mathbf{k}_0 \pm \mathbf{Q}$ is

$$\frac{A_{-\mathbf{k}_0}}{A_{-\mathbf{k}_0 \pm \mathbf{Q}}} = \frac{0.828}{0.388} = 2.13, \quad (\text{B4})$$

and the ratio between the peaks at $-\mathbf{k}_0$ and $-\mathbf{k}_0 \pm 2\mathbf{Q}$ is

$$\frac{A_{-\mathbf{k}_0}}{A_{-\mathbf{k}_0 \pm 2\mathbf{Q}}} = \frac{0.828}{0.0786} = 10.53, \quad (\text{B5})$$

while the ratios obtained from the simulations of the GPE are [results of Figs. 7(a) and 7(e)]

$$\left(\frac{A_{-\mathbf{k}_0}}{A_{-\mathbf{k}_0 \pm \mathbf{Q}}} \right) \approx 2.15, \quad \left(\frac{A_{-\mathbf{k}_0}}{A_{-\mathbf{k}_0 \pm 2\mathbf{Q}}} \right) \approx 10.19. \quad (\text{B6})$$

These two values match exactly with the results based on the five-band model. We need to point out that if we consider the three-band model used in the main text, the ratio $\frac{A_{-\mathbf{k}_0}}{A_{-\mathbf{k}_0 \pm \mathbf{Q}}} = 2.29$, which is slightly poorer than the five-band model. In experiments, this ratio can be directly obtained from the time-of-flight measurement.

-
- [1] M. Z. Hasan and C. L. Kane, Colloquium: Topological insulators, *Rev. Mod. Phys.* **82**, 3045 (2010).
- [2] X.-L. Qi and S.-C. Zhang, Topological insulators and superconductors, *Rev. Mod. Phys.* **83**, 1057 (2011).
- [3] J. Sinova, S. O. Valenzuela, J. Wunderlich, C. H. Back, and T. Jungwirth, Spin Hall effects, *Rev. Mod. Phys.* **87**, 1213 (2015).
- [4] D. Xiao, M.-C. Chang, and Q. Niu, Berry phase effects on electronic properties, *Rev. Mod. Phys.* **82**, 1959 (2010).
- [5] V. Galitski and I. B. Spielman, Spin-orbit coupling in quantum gases, *Nature* **494**, 49 (2013).
- [6] B. K. Stuhl, H.-I. Lu, L. M. Ayccock, D. Genkina, and I. B. Spielman, Visualizing edge states with an atomic Bose gas in the quantum Hall regime, *Science* **349**, 1514 (2015).
- [7] H. Zhai, Degenerate quantum gases with spin-orbit coupling: A review, *Rep. Prog. Phys.* **78**, 026001 (2015).
- [8] Z. Fu, L. Huang, Z. Meng, P. Wang, L. Zhang, S. Zhang, H. Zhai, P. Zhang, and J. Zhang, Production of Feshbach molecules induced by spin-orbit coupling in Fermi gases, *Nat. Phys.* **10**, 110 (2013).
- [9] M. L. Wall, A. P. Koller, S. Li, X. Zhang, N. R. Cooper, J. Ye, and A. M. Rey, Synthetic Spin-Orbit Coupling in an Optical Lattice Clock, *Phys. Rev. Lett.* **116**, 035301 (2016).
- [10] S. Kolkowitz, S. L. Bromley, T. Bothwell, M. L. Wall, G. E. Marti, A. P. Koller, X. Zhang, A. M. Rey, and J. Ye, Spin-orbit-coupled fermions in an optical lattice clock, *Nature* **542**, 66 (2017).
- [11] M. H. Anderson, J. R. Ensher, M. R. Matthews, C. E. Wieman, and E. A. Cornell, Observation of Bose-Einstein condensation in a dilute atomic vapor, *Science* **269**, 198 (1995).

- [12] C. C. Bradley, C. A. Sackett, J. J. Tollett, and R. G. Hulet, Evidence of Bose-Einstein Condensation in an Atomic Gas with Attractive Interactions, *Phys. Rev. Lett.* **75**, 1687 (1995).
- [13] C. Wang, C. Gao, C.-M. Jian, and H. Zhai, Spin-Orbit Coupled Spinor Bose-Einstein Condensates, *Phys. Rev. Lett.* **105**, 160403 (2010).
- [14] Y. Li, L. P. Pitaevskii, and S. Stringari, Quantum Tricriticality and Phase Transitions in Spin-Orbit Coupled Bose-Einstein Condensates, *Phys. Rev. Lett.* **108**, 225301 (2012).
- [15] J.-R. Li, J. Lee, W. Huang, S. Burchesky, B. Shteynas, F. Ç. Top, A. O. Jamison, and W. Ketterle, A stripe phase with supersolid properties in spin-orbit-coupled Bose-Einstein condensates, *Nature* **543**, 91 (2017).
- [16] C.-H. Li, C. Qu, R. J. Niffenegger, S.-J. Wang, M. He, D. B. Blasing, A. J. Olson, C. H. Greene, Y. Lyanda-Geller, Q. Zhou, C. Zhang, and Y. P. Chen, Spin current generation and relaxation in a quenched spin-orbit-coupled Bose-Einstein condensate, *Nat. Commun.* **10**, 1 (2019).
- [17] L. Fu and C. L. Kane, Superconducting Proximity Effect and Majorana Fermions at the Surface of a Topological Insulator, *Phys. Rev. Lett.* **100**, 096407 (2008).
- [18] N. R. Cooper and G. V. Shlyapnikov, Stable Topological Superfluid Phase of Ultracold Polar Fermionic Molecules, *Phys. Rev. Lett.* **103**, 155302 (2009).
- [19] Y. Oreg, G. Refael, and F. von Oppen, Helical Liquids and Majorana Bound States in Quantum Wires, *Phys. Rev. Lett.* **105**, 177002 (2010).
- [20] R. M. Lutchyn, J. D. Sau, and S. Das Sarma, Majorana Fermions and a Topological Phase Transition in Semiconductor-Superconductor Heterostructures, *Phys. Rev. Lett.* **105**, 077001 (2010).
- [21] J. Zhou, W. Zhang, and W. Yi, Topological superfluid in a trapped two-dimensional polarized Fermi gas with spin-orbit coupling, *Phys. Rev. A* **84**, 063603 (2011).
- [22] V. Mourik, K. Zuo, S. M. Frolov, S. R. Plissard, E. P. A. M. Bakkers, and L. P. Kouwenhoven, Signatures of Majorana fermions in hybrid superconductor-semiconductor nanowire devices, *Science* **336**, 1003 (2012).
- [23] A. Yu Kitaev, Unpaired Majorana fermions in quantum wires, *Phys. Usp.* **44**, 131 (2001).
- [24] S. Tewari, S. Das Sarma, C. Nayak, C. Zhang, and P. Zoller, Quantum Computation using Vortices and Majorana Zero Modes of a $p_x + ip_y$ Superfluid of Fermionic Cold Atoms, *Phys. Rev. Lett.* **98**, 010506 (2007).
- [25] H.-H. Sun, K.-W. Zhang, L.-H. Hu, C. Li, G.-Y. Wang, H.-Y. Ma, Z.-A. Xu, C.-L. Gao, D.-D. Guan, Y.-Y. Li, C. Liu, D. Qian, Y. Zhou, L. Fu, S.-C. Li, F.-C. Zhang, and J.-F. Jia, Majorana Zero Mode Detected with Spin Selective Andreev Reflection in the Vortex of a Topological Superconductor, *Phys. Rev. Lett.* **116**, 257003 (2016).
- [26] D. Hsieh, D. Qian, L. Wray, Y. Xia, Y. S. Hor, R. J. Cava, and M. Z. Hasan, A topological Dirac insulator in a quantum spin Hall phase, *Nature* **452**, 970 (2008).
- [27] D. Pesin and L. Balents, Mott physics and band topology in materials with strong spin-orbit interaction, *Nat. Phys.* **6**, 376 (2010).
- [28] M. Gong, S. Tewari, and C. Zhang, BCS-BEC Crossover and Topological Phase Transition in 3D Spin-Orbit Coupled Degenerate Fermi Gases, *Phys. Rev. Lett.* **107**, 195303 (2011).
- [29] B. Huang, C. F. Chan, and M. Gong, Large Chern-number topological superfluids in a coupled-layer system, *Phys. Rev. B* **91**, 134512 (2015).
- [30] Y.-J. Lin, K. Jiménez-García, and I. B. Spielman, Spin-orbit-coupled Bose-Einstein condensates, *Nature* **471**, 83 (2011).
- [31] Z. Wu, L. Zhang, W. Sun, X.-T. Xu, B.-Z. Wang, S.-C. Ji, Y. Deng, S. Chen, X.-J. Liu, and J.-W. Pan, Realization of two-dimensional spin-orbit coupling for Bose-Einstein condensates, *Science* **354**, 83 (2016).
- [32] L. Huang, Z. Meng, P. Wang, P. Peng, S.-L. Zhang, L. Chen, D. Li, Q. Zhou, and J. Zhang, Experimental realization of two-dimensional synthetic spin-orbit coupling in ultracold Fermi gases, *Nat. Phys.* **12**, 540 (2016).
- [33] S.-L. Zhu, H. Fu, C.-J. Wu, S.-C. Zhang, and L.-M. Duan, Spin Hall Effects for Cold Atoms in a Light-Induced Gauge Potential, *Phys. Rev. Lett.* **97**, 240401 (2006).
- [34] I. B. Spielman, Raman processes and effective gauge potentials, *Phys. Rev. A* **79**, 063613 (2009).
- [35] X.-J. Liu, M. F. Borunda, X. Liu, and J. Sinova, Effect of Induced Spin-Orbit Coupling for Atoms via Laser Fields, *Phys. Rev. Lett.* **102**, 046402 (2009).
- [36] B. M. Anderson, G. Juzeliūnas, V. M. Galitski, and I. B. Spielman, Synthetic 3D Spin-Orbit Coupling, *Phys. Rev. Lett.* **108**, 235301 (2012).
- [37] J.-Y. Zhang, S.-C. Ji, Z. Chen, L. Zhang, Z.-D. Du, B. Yan, G.-S. Pan, B. Zhao, Y.-J. Deng, H. Zhai, S. Chen, and J.-W. Pan, Collective Dipole Oscillations of a Spin-Orbit Coupled Bose-Einstein Condensate, *Phys. Rev. Lett.* **109**, 115301 (2012).
- [38] P. Wang, Z.-Q. Yu, Z. Fu, J. Miao, L. Huang, S. Chai, H. Zhai, and J. Zhang, Spin-orbit Coupled Degenerate Fermi Gases, *Phys. Rev. Lett.* **109**, 095301 (2012).
- [39] C. Hamner, C. Qu, Y. Zhang, JiaJia Chang, M. Gong, C. Zhang, and P. Engels, Dicke-type phase transition in a spin-orbit-coupled Bose-Einstein condensate, *Nat. Commun.* **5**, 4023 (2014).
- [40] S.-C. Ji, J.-Y. Zhang, L. Zhang, Z.-D. Du, W. Zheng, Y.-J. Deng, H. Zhai, S. Chen, and J.-W. Pan, Experimental determination of the finite-temperature phase diagram of a spin-orbit coupled Bose gas, *Nat. Phys.* **10**, 314 (2014).
- [41] A. J. Olson, S.-J. Wang, R. J. Niffenegger, C.-H. Li, C. H. Greene, and Y. P. Chen, Tunable Landau-Zener transitions in a spin-orbit-coupled Bose-Einstein condensate, *Phys. Rev. A* **90**, 013616 (2014).
- [42] J. Li, W. Huang, B. Shteynas, S. Burchesky, F. C. Top, E. Su, J. Lee, A. O. Jamison, and W. Ketterle, Spin-Orbit Coupling and Spin Textures in Optical Superlattices, *Phys. Rev. Lett.* **117**, 185301 (2016).
- [43] A. Aspect, E. Arimondo, R. Kaiser, N. Vansteenkiste, and C. Cohen-Tannoudji, Laser Cooling below the One-Photon Recoil Energy by Velocity-Selective Coherent Population Trapping, *Phys. Rev. Lett.* **61**, 826 (1988).
- [44] C. Kittel, *Introduction to Solid State Physics*, 8th ed. (Wiley, Hoboken, NJ, 2005).
- [45] Y. Ando, Topological insulator materials, *J. Phys. Soc. Jpn* **82**, 102001 (2013).
- [46] G. Dresselhaus, Spin-orbit coupling effects in zinc blende structures, *Phys. Rev.* **100**, 580 (1955).
- [47] G. Bihlmayer, O. Rader, and R. Winkler, Focus on the Rashba effect, *New J. Phys.* **17**, 050202 (2015).

- [48] S. Inouye, M. R. Andrews, J. Stenger, H.-J. Miesner, D. M. Stamper-Kurn, and W. Ketterle, Observation of Feshbach resonances in a Bose-Einstein condensate, *Nature* **392**, 151 (1998).
- [49] W. Zheng and Z. Li, Collective modes of a spin-orbit-coupled Bose-Einstein condensate: A hydrodynamic approach, *Phys. Rev. A* **85**, 053607 (2012).
- [50] X.-L. Chen, J. Wang, Y. Li, X.-J. Liu, and H. Hu, Quantum depletion and superfluid density of a supersolid in Raman spin-orbit-coupled Bose gases, *Phys. Rev. A* **98**, 013614 (2018).
- [51] Y. Li, G. I. Martone, L. P. Pitaevskii, and S. Stringari, Superstripes and the Excitation Spectrum of a Spin-Orbit-Coupled Bose-Einstein Condensate, *Phys. Rev. Lett.* **110**, 235302 (2013).
- [52] L. N. Cooper, Bound electron pairs in a degenerate Fermi gas, *Phys. Rev.* **104**, 1189 (1956).
- [53] J. Bardeen, L. N. Cooper, and J. R. Schrieffer, Microscopic theory of superconductivity, *Phys. Rev.* **106**, 162 (1957).
- [54] F. Wu, G.-C. Guo, W. Zhang, and W. Yi, Unconventional Superfluid in a Two-Dimensional Fermi Gas with Anisotropic Spin-Orbit Coupling and Zeeman Fields, *Phys. Rev. Lett.* **110**, 110401 (2013).
- [55] C. Qu, M. Gong, and C. Zhang, Fulde-Ferrell-Larkin-Ovchinnikov or Majorana superfluids: The fate of fermionic cold atoms in spin-orbit-coupled optical lattices, *Phys. Rev. A* **89**, 053618 (2014).
- [56] W. V. Liu, Theoretical Study of the Damping of Collective Excitations in a Bose-Einstein Condensate, *Phys. Rev. Lett.* **79**, 4056 (1997).
- [57] S. Giorgini, Damping in dilute bose gases: A mean-field approach, *Phys. Rev. A* **57**, 2949 (1998).
- [58] R. Wu and Z. Liang, Beliaev Damping of a Spin-Orbit-Coupled Bose-Einstein Condensate, *Phys. Rev. Lett.* **121**, 180401 (2018).
- [59] F. M. Cucchiatti and E. Timmermans, Strong-Coupling Polarons in Dilute Gas Bose-Einstein Condensates, *Phys. Rev. Lett.* **96**, 210401 (2006).
- [60] M.-G. Hu, M. J. Van de Graaff, D. Kedar, J. P. Corson, E. A. Cornell, and D. S. Jin, Bose Polarons in the Strongly Interacting Regime, *Phys. Rev. Lett.* **117**, 055301 (2016).
- [61] Y. E. Shchadilova, R. Schmidt, F. Grusdt, and E. Demler, Quantum Dynamics of Ultracold Bose Polarons, *Phys. Rev. Lett.* **117**, 113002 (2016).
- [62] D. A. Steck, Rubidium 87 D line data (revision 2.1.5), available at <http://steck.us/alkalidata> (13 January 2015).
- [63] J. J. Sakurai, *Advanced Quantum Mechanics* (Addison-Wesley, Reading, MA, 1998).